nature communications

Article

https://doi.org/10.1038/s41467-026-72281-3

Speckle-based measurement of the fractional azimuthal index of orbital angular momentum beams for refractive index sensing

Received: 14 September 2025

Accepted: 13 April 2026

Published online: 08 May 2026

Check for updates

Christopher Perrella[1,2,3,10], Aman Anil Punse[1,2,3,10], Anastasiia Zalogina[1,2,4], Crispin Szydzik[5,6], Megan Lim[1,2,7], Andreas Boes[2,3,8], Arnan Mitchell[5,6], Kylie R. Dunning[1,2,7] & Kishan Dholakia[1,2,3,9]

Light beams possessing orbital angular momentum (OAM) have gained significant interest in areas such as optical manipulation, quantum entanglement, and super-resolved imaging. The OAM per photon of such beams, typically Laguerre-Gaussian beams, is directly proportional to the azimuthal index l. This index is continuous in nature and a non-trivial parameter to measure. In this study, Laguerre-Gaussian beams of differing l are generated through mode conversion using microscopic spiral phase plates. The value of l depends on the refractive index of the medium surrounding the spiral phase plates. Utilising laser speckle, we demonstrate an ultra-precise measurement of the azimuthal index of the generated beams to a precision of 2×10^{-5}. In turn, this enables an ultra-precise measurement of the refractive index of the medium surrounding the spiral phase plates, with a best measured precision of 6.4×10^{-7} refractive index units. Our study interrogates samples of sucrose and haemoglobin, only 300 pL in volume, within a microfluidic channel.

Light fields possessing orbital angular momentum have become a mainstay for a diverse range of key research areas in the last few decades[1–3]. The fundamental properties and evolution of such beams is also topic of major interest[4,5]. Such fields may have a phase singularity (vortex) embedded within the field. The orbital component of the angular momentum arises from inclined wavefronts that lead to a spiralling motion of the energy flow (Poynting vector) of the beam[1,4,6]. This is distinct from the spin angular momentum of a light field, which is associated with the polarisation state of the beam. A prime example of light fields with orbital angular momentum are the cylindrically symmetric Laguerre–Gaussian (LG) transverse modes[1,4]. The transverse mode of a LG beam is described by two indices with the azimuthal index, l, garnering the most interest[1]. This index quantifies the amount of phase accumulation, of $2\pi l$, around the mode circumference[1]. Such fields have an orbital angular momentum of $l\hbar$ per photon.

Applications for LG modes have been found in many areas, including optical manipulation of atoms and mesoscopic particles[7],

[1]Centre of Light for Life, School of Biological Sciences, Adelaide University, Adelaide, SA, Australia. [2]Institute for Photonics and Advanced Sensing, Adelaide University, Adelaide, SA, Australia. [3]ARC Centre of Excellence in Optical Microcombs for Breakthrough Science (COMBS), Adelaide University, Adelaide, SA, Australia. [4]Quantum Materials and Nanophotonics, School of Mathematical and Physical Sciences, University of Technology Sydney, Sydney, NSW, Australia. [5]ARC Centre of Excellence in Optical Microcombs for Breakthrough Science (COMBS), RMIT University, Melbourne, VIC, Australia. [6]Integrated Photonics and Applications Centre, School of Engineering, RMIT University, Melbourne, VIC, Australia. [7]Robinson Research Institute, School of Biomedicine, Adelaide University, Adelaide, SA, Australia. [8]School of Electrical and Mechanical Engineering, Adelaide University, Adelaide, SA, Australia. [9]SUPA, School of Physics and Astronomy, University of St Andrews, St Andrews, UK. [10]These authors contributed equally: Christopher Perrella, Aman Anil Punse.
e-mail: kishan.dholakia@adelaide.edu.au

where they lead to rotation of trapped structures, optical communication[8,9], where they can enhance data transmission security, and quantum communication[10,11], where they offer access to a higher-dimensional Hilbert space enabling more efficient use of communication channels. Furthermore, the LG mode with $l = 1$ is central to super-resolution microscopy[12] where the singularity at the centre of the beam is exploited to improve resolution to achieve nanometre level imaging[13,14].

Though most of the interest has focused on LG beams with integer values of l, there does not need to be a multiple of 2π around the mode circumference. These light fields may possess a non-integer, or fractional, azimuthal index. Such fields may be decomposed into combinations of LG modes with integer azimuthal indices of varying amplitude[15]. Therefore, the azimuthal index is in fact a continuous value and may take on any value.

A precise measurement of the azimuthal index, l, is a pertinent requirement in a number of the aforementioned applications[2,8,16]. The determination of the azimuthal index of LG modes has been explored at both the classical and single-photon level[17–20]. Typical methods for determining the azimuthal index of a beam include: diffraction from an aperture[21,22], modified Mach–Zehnder interferometers[20,23–25], and more recently, statistical analysis or machine learning[26,27]. For classical beams, the majority of these methods focus on determining integer l and typically find it challenging to measure fractional l. The most precise measurements to date for measuring fractional azimuthal index l may resolve changes to an accuracy of 0.01 using deep learning[26], and 0.05 when using interference fringe dislocation[28]. A summary table on previous literature[22–24,26–32] is provided in the Supplementary Table 6. Measurement beyond this precision remains a highly desirable, but unresolved, goal.

Here, we focus on the precision measurement of l, which is based on light propagation through disordered media resulting in speckle patterns. Speckle patterns are generally regarded as a randomisation process of the optical field and have been viewed as deleterious to optical measurements, destroying information contained within the light field. However, these interference patterns are deterministic and rich in information about the source of light, disordered medium and environment[33–38]. Speckle patterns are based on interference. However, their high-dimensional nature, arising from the interference of many field components, provides rich information content that enables high-precision measurements. Furthermore, these patterns do not repeat like traditional interferometric fringe patterns, enabling measurements over a large dynamic range without the need for a reference arm. While analysis of light fields possessing OAM has already been investigated[39,40], it has mainly focused on demonstrating classification of light fields with integer azimuthal indices[41–44]. Here, we advance the precision of azimuthal index measurements using this innovative approach of speckle metrology, measuring non-integer values of the azimuthal index to an unprecedented measurement precision of l of 2×10^{-5}, a three-order of magnitude improvement in comparison to other methods. In itself, this significant advance may allow for a higher density and increased data transfer rates in optical communications[15], and enhanced manipulation and control of the motion of trapped mesoscopic particles.

In this study, we exploit this precision measurement of azimuthal index to realise a novel approach to measure refractive index. Our method of LG beam generation involves mode conversion with a microscopic spiral phase plate (SPP) immersed in the medium of interest within a microfluidic channel. Our approach samples a volume of 300 pL. The mode conversion is dependent upon the refractive index of both the plate and the surrounding environment. Thus, we leverage our speckle-based measurement of l to, in turn, determine the refractive index of a liquid sample surrounding the SPP, with a best measured precision of 6.4×10^{-7} refractive index units (RIU), which is at the shot-noise limit of the system. We note that schemes have been used for refractive index sensing in bulk media, using the interference patterns of an LG beam with a co-aligned reference beam[45–48]. Precisions of 5×10^{-6} RIU[47] and 3.46×10^{-7} RIU[48] have been reported. A more detailed summary of these works[45–50] can be found in Supplementary Table 5. In contrast to these studies, our approach is based on a direct measurement of the LG beam, obviating the need for any reference field for interference. To minimise the volume of sample required for testing, we utilise a microfluidic environment with 50 µm diameter SPPs, allowing refractive index sensing of picolitre sample volumes. The direct nature of our measurement has multiple advantages: it obviates the requirement of a reference beam and thus alignment of an interferometer, interrogates picolitre volumes (rather than a bulk measurement), and may be readily multiplexed within the microfluidic chamber.

At the heart of our sensing approach is mode conversion of a Gaussian beam to a LG beam and subsequent determination of the azimuthal phase accrued in the process. We achieve this by imparting an azimuthally varying wavefront phase retardation upon an input Gaussian beam[51–53], using a microfabricated SPP, shown in Fig. 1a, b, a scanning electron microscope image of which is shown in Fig. 1c). These SPPs create LG beams with an azimuthal index, l and a radial index of $p = 0$, see Fig. 1a) (inset).

After passing through the SPP, the azimuthal phase, ϕ, accumulated around the beam is given by the difference in optical path length accrued around the wavefront, given by $\phi = 2\pi h_s(n_{SPP} - n)/\lambda_0$ for a laser with a vacuum wavelength of λ_0 passing through a SPP of refractive index n_{SPP} with a step height h_s (see Fig. 1c), surrounded by a sample liquid of refractive index n. Thus, the azimuthal index of the generated beam is:

$$l = \frac{\phi}{2\pi} = \frac{h_s(n_{SPP} - n)}{\lambda_0}. \quad (1)$$

It should be noted that this is a change to the azimuthal index of the beam, that is a beam starting with an azimuthal index of l_0 would have an azimuthal index of $l_0 + l$ after the SPP mode conversion. The input beam here is a Gaussian ($l = 0$) mode, thus the generated beam simply has an azimuthal index of l. Precise measurement of the azimuthal index, l, of the generated LG beam allows calculation of the refractive index of the sample via:

$$n = n_{SPP} - \frac{l\lambda}{h_s}, \quad (2)$$

allowing us to measure the refractive index of the sample media surrounding the SPP.

Figure 1a shows the experimental diagram in which a laser with an input Gaussian spatial profile passes through an SPP, transforming it into a LG beam. The refractive index of the sample surrounding the SPP, n, determines the azimuthal index of the generated LG beam. We use speckle metrology to precisely measure the azimuthal index of the beam, whereby a speckle pattern is generated via a diffuser then imaged on a camera. A diffuser is used as it scatters the beam once, which is sufficient to extract maximum information regarding the spatial mode of a beam[54]. This is in contrast to path-dependent measurements, such as wavelength or displacement, that gain sensitivity from multiple scattering events, utilising multimode fibre or integrating spheres to produce speckle patterns. The benefit of utilising a single scatterer, such as a diffuser, is that it minimises the speckle measurement sensitivity to these other quantities, wavelength or displacement. Principal component analysis (PCA) is utilised to extract the azimuthal index of the generated beam, and refractive index of the sample, the method of which is discussed in the "Methods" section, and theoretical analysis of the process presented in the Supplementary Information, Section 1. In summary, a set of speckle images is required

https://doi.org/10.1038/s41467-026-72281-3

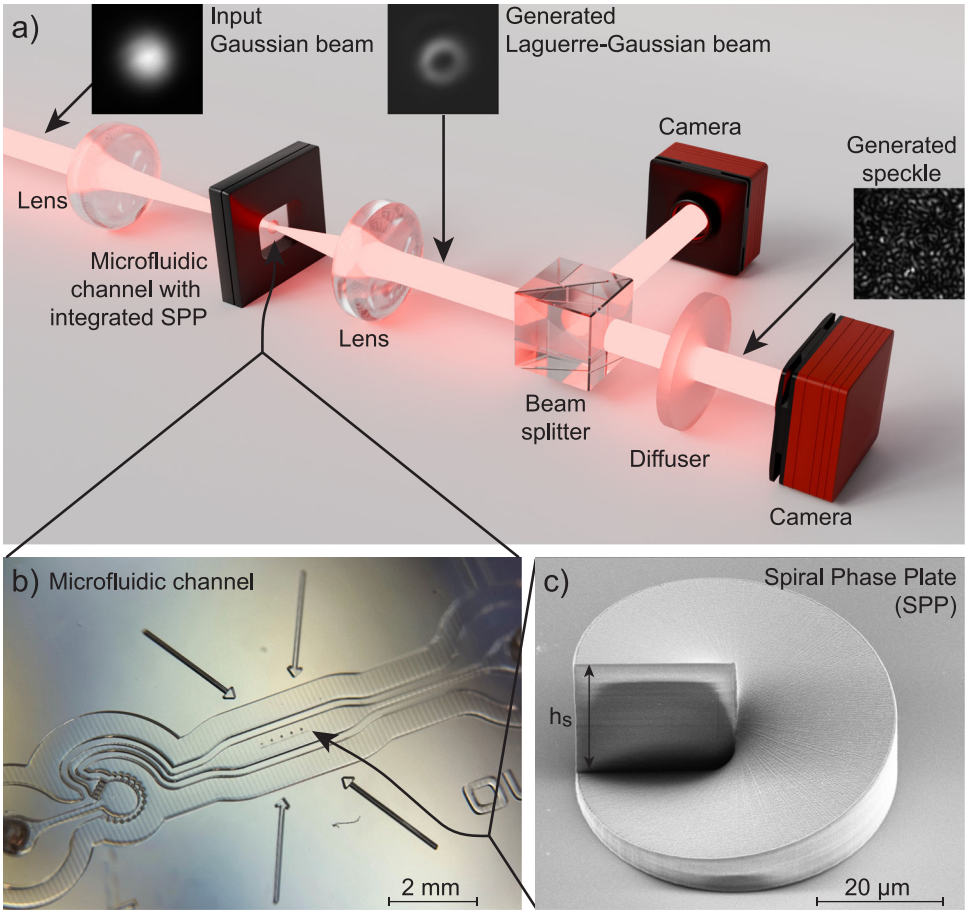

Fig. 1 | Experimental diagram showing the speckle measurement of azimuthal and refractive index. a Experimental diagram showing a Gaussian beam passing through an SPP, transforming it into a Laguerre–Gaussian (LG) beam. The presence of liquid samples of differing refractive index around the SPP changes the resultant azimuthal index of the beam. To accurately measure the azimuthal index of the resultant beam, a speckle pattern is generated using a diffuser and imaged on a camera. The intensity profile of the LG beam prior to the diffuser is also imaged using a camera for reference. **b** Shows a microscope image of the microfluidic chip with the SPPs at the centre. **c** Shows a scanning electron microscope image of one of the SPPs and its dimensions. The height of the phase plate step is denoted h_s.

at known azimuthal/refractive indices to calibrate the PCA, after which the azimuthal index of an unknown LG beam, or the refractive index of an unknown sample, can then be measured. It is not necessary to measure every azimuthal index value. Rather, we may interpolate between calibration points in PCA space to determine the value of l[34]. The noise limit of our measurement is discussed in detail in the Supplementary Information, Section 4.

Results

Measurement precision

We test the precision of our method at two different wavelengths of 1064 and 532 nm, with two different SPPs with heights of $h_s = 10.34$ µm and $h_s = 25.85$ µm, designed to generate LG beams with azimuthal index of $l = 2$ and $l = 5$, respectively, in heavy-water D_2O at a design wavelength of 1064 nm (refractive index $n = 1.3211$[55]). These SPPs are referred to as SPP2 and SPP5, respectively. We have fabricated SPPs that generate $l = 1$ to $l = 5$ at 1064 nm, or $l \approx 2$ to $l \approx 10$ at 532 nm. We focus on SPP2 and SPP5 in this study to demonstrate the capability of the approach, with higher azimuthal indices chosen to enhance measurement precision, as discussed below.

The following procedure was used to determine the measurement precision of both the azimuthal and refractive index. For each SPP, the system was calibrated for refractive indices between 1.3328 and 1.3403 for which sucrose samples were used (0–5% sucrose solution), although any refractive index range can be chosen. Following calibration, precision measurements were taken to ascertain the azimuthal and refractive index measurement precision. Eight solutions within the calibration refractive index range were chosen, four of which were at the same refractive index as the calibration set, and four that were not. For each of these eight solutions, $N = 10$ measurements of azimuthal and refractive index were made, the standard deviation of which gives an indication of the precision of each measurement. This process, of calibration followed by eight precision measurements, is replicated 4–5 times, giving approximately $N = 32$–40 precision measurements for a single plate. Averaging over the $N = 32$–40 precision measurements gives an average precision for the azimuthal and refractive index measurements for each plate. The averaged precision is presented with errors, which are the standard error in the mean of these measurements.

Figure 2a, b shows a single replicate of calibration and azimuthal and refractive index precision measurements for SPP2 and SPP5, respectively. The calibration data fall around the line of expectation (grey), with the precision tests clumping tightly ($N = 10$ measurements at each refractive index). The error bars are based upon the measurement accuracy of the commercial refractometer ($\pm 3 \times 10^{-4}$ RIU) used to determine the refractive index of the calibration solution (MyBrix, Mettler Toledo). To better illustrate the excellent measurement precision, residuals are displayed showing the difference between the measurements and the expected values, from which minimal deviation from the expected values is observed.

https://doi.org/10.1038/s41467-026-72281-3

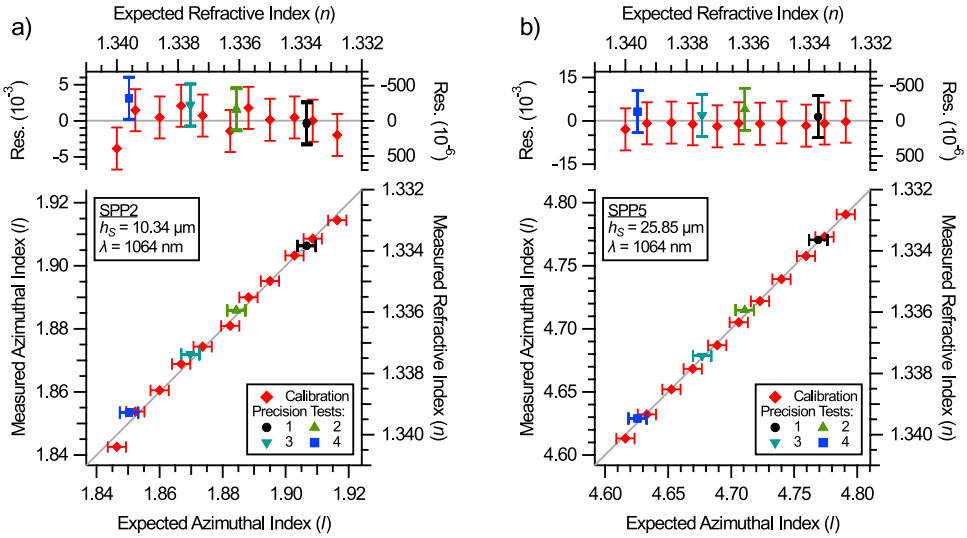

Fig. 2 | Azimuthal index and refractive index precision measurements. Measured azimuthal index as a function of the expected azimuthal index, as well as the extracted refractive index measurements. The upper panel shows the precision of the measurements by presenting residuals between the measurements and the expected values. **a** Measurements for SPP2 with a plate height $h_s = 10.34$ µm at wavelength $\lambda = 1064$ nm. **b** Measurements for SPP5 with a plate height $h_s = 25.85$ µm at wavelength $\lambda = 1064$ nm. Each calibration point comprises of one sample ($N = 1$). The precision tests (denoted 1–4) correspond to four measurements made at different refractive indices relative to the calibration set. This highlights the capability of the PCA analysis to interpolate between calibration points. Each precision test (denoted 1–4) consists of $N = 10$ measurements of the same sample. All $N = 10$ measurements are plotted, however, they cannot be individually seen as they all overlap, highlighting the high precision of the speckle measurements. The error bars represent the measurement accuracy of the commercial refractometer ($\pm 3 \times 10^{-4}$ RIU). It can be seen that near all measurements agree to the expected value (gray line) within the accuracy of the commercial refractometer.

At an input wavelength of 1064 nm, for SPP2, an average refractive index precision of $(7.4 \pm 0.5) \times 10^{-6}$ RIU was achieved, from which SPP5 improved upon, achieving an average precision of $(3.4 \pm 0.4) \times 10^{-6}$ RIU. The best precisions measured for each plate were 3.3×10^{-6} and 0.7×10^{-6} RIU for SPP2 and SPP5, respectively. The precision of the system is expected to increase linearly with plate height, h_s as described by Eq. 1, and discussed in more detail in the Supplementary Information, Section 2.1. Thus, we expect an increase in the precision of SPP5 compared to SPP2 of 2.5-fold based on their respective heights of $h_s = 25.85$ µm and $h_s = 10.34$ µm. Our measured precisions give an average ratio of 2.2 ± 0.3 between the two plates, which agrees well with expectation. The refractive index precision is limited by shot noise of the detected light, discussed in detail in Supplementary Information, Section 4.3.

At 1064 nm for both SPP2 and SPP5, the average precision of the azimuthal index measurements, respectively, is $(7.2 \pm 0.5) \times 10^{-5}$ and $(8.6 \pm 1.0) \times 10^{-5}$. The best precision of the azimuthal index measurements is 3.2×10^{-5} and 1.8×10^{-5} for the SPP2 and SPP5, respectively. With increasing azimuthal index, l, the grain size of the speckle pattern reduces[56,57]. In path-dependent speckle measurements, such as wavelength or displacement measurements, a finer grain size typically leads to higher measurement sensitivity[54]. However, for azimuthal index measurements, the sensitivity of the speckle measurement to changes in azimuthal index is independent of speckle grain size, thus the magnitude of the azimuthal index[54] remains constant, further details can be found in the Supplementary Information, Section 1. This is observed in the ratio of the measured azimuthal index precisions between SPP2 and SPP5 to be 0.9 ± 0.1, in line with the expected ratio of 1.

The average refractive index precision is further improved by moving to a shorter input wavelength, leading to a larger phase shift being accrued around the beam circumference after passing through the SPP, leading to a generated beam with a higher azimuthal index. This is seen by the $1/\lambda$ proportionality in Eq. 1, and discussed in more detail in the Supplementary Information, Section 2.2. Figure 3 shows the calibration and precision measurements for SPP5 at the input wavelength of 532 nm. For SPP5, at 532 nm, an average precision of $(2.2 \pm 0.3) \times 10^{-6}$ RIU was achieved, with the best precision observed being 0.64×10^{-6}. When compared to the 1064 nm SPP5 results, we expect a two-fold improvement in precision using 532 nm due to the $1/\lambda$ proportionality in Eq. 1. This is discussed in more detail in the Supplementary Information, Section 2.2. Comparing measured precisions for SPP5 at 532 and 1064 nm, we observe a ratio of 1.6 ± 0.3, which agrees well with expectation.

At 532 nm, for SPP5, the average precision of the azimuthal index is $(10.6 \pm 1.7) \times 10^{-5}$, with the best measurement being 3.1×10^{-5}. To our knowledge, these measurements for the fractional azimuthal index are the most precise to date. Similar to the expected azimuthal index precision ratio between SPP2 and SPP5 at 1064 nm discussed above, we also expect an azimuthal index precision ratio of 1 between SPP5 at 1064 nm and SPP5 at 532 nm, for which we measured a ratio of 0.8 ± 0.2 in line with these expectations.

Precise refractive index measurements of haemoglobin

To validate the applicability of the system, we performed precision measurements on ultra-low volumes of a biological sample, namely haemoglobin. The volume of the sample needed to fill the microfluidic chamber containing multiple SPPs (seen in Fig. 1b) is only 22 µL. However, the sample volume that the light traverses through is only 300 pL, given by the chamber height of 160 µm, and 50 µm diameter of a SPP. In future, the chamber size could be reduced considerably to accommodate a single SPP, reducing the sample volume towards the picolitre regime or lower, which is considered in more detail in the discussion section below.

In a biological context, precise refractive index measurements have been applied to protein characterisation studies by determining the protein refractive index increment[58]. The precise measurement of protein refractive index has significant applications as a non-destructive form of protein analysis in a range of industries, such as food and beverage, as well as pharmaceutical drug testing[59,60]. Recently, the refractive index increment of low concentrations of protein was measured using precision interferometry to study their

https://doi.org/10.1038/s41467-026-72281-3

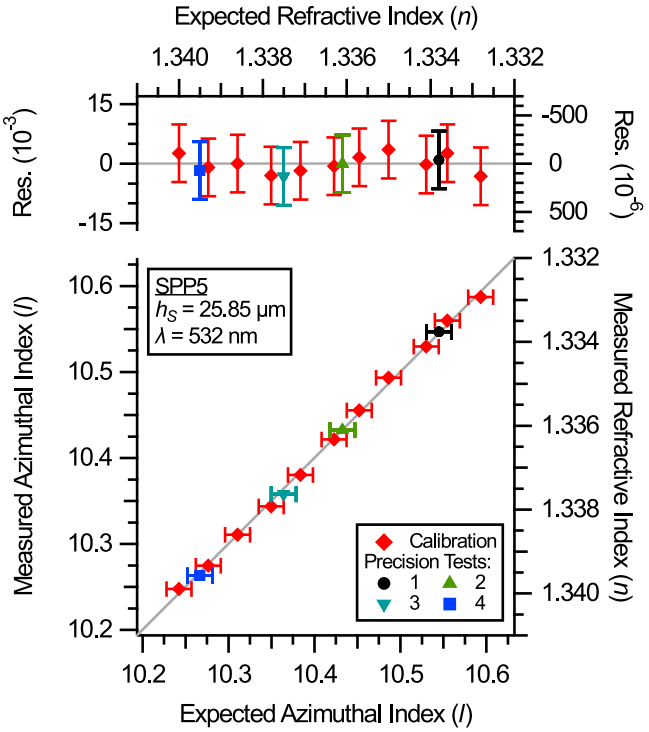

Fig. 3 | Azimuthal index and refractive index precision measurements at 532 nm. Measurements at a wavelength of $\lambda = 532$ nm showing measured azimuthal index as a function of the expected azimuthal index, as well as the extracted refractive index. The upper panel shows the precision of the measurements by presenting residuals between the measurements and the expected values. Measurements for SPP5 with a plate height $h_s = 25.85$ µm. Each calibration point comprises of one sample ($N = 1$). The precision tests (denoted 1–4) correspond to four measurements made at different refractive indices relative to the calibration set. Each precision test (denoted 1–4) consists of $N = 10$ measurements of the same sample. All $N = 10$ measurements are plotted, however, they cannot be individually seen as they all overlap. The error bars represent the measurement accuracy of the commercial refractometer ($\pm 3 \times 10^{-4}$ RIU).

conformational state[61]. It is worth noting the use of interferometry to measure refractive index differs from our described methods.

To test our system in a biological setting, we first calibrated the system using sucrose solution, then measured the refractive index of three biological samples. Figure 4 shows results using SPP5 at 1064 nm. We note that similar results were obtained using SPP2 at 1064 nm. In our case, these samples were two different concentrations of haemoglobin (0.3 mmol/L and 0.5 mmol/L), which were dissolved in a PBS (phosphate-buffered saline) buffer, with a blank PBS buffer being the third solution. The refractive index measured for the biological sample was within 0.02% of the actual value, as measured by the commercial refractometer, as seen in Fig. 4. This demonstrates that by using our speckle-based measurements of azimuthal index, we could accurately determine the refractive index of any unknown biological sample to a very high precision.

Discussion

We have demonstrated ultra-precise measurement of the fractional azimuthal index of a LG beam to a precision of 2×10^{-5} using speckle metrology. This precision exceeds the previous best azimuthal index measurement by over three orders of magnitude, with a summary of previous studies being found in Supplementary Table 6. This advancement will significantly impact fields that utilise OAM, such as optical communication, and in applications that utilise optical manipulation of atoms and mesoscopic particles, this may lead to finer control of trapped particles/structures.

As part of our study, we demonstrated the ability to create LG beams with finely controlled azimuthal index, with minimum step size of 0.002. Here, the concentration of the sucrose solution surrounding the SPP determined the azimuthal index of the generated beam. Typically, a spatial light modulator (SLM) is used to create beams with variable azimuthal index. However, we remark that the minimum azimuthal index step size demonstrated here of 0.002 requires a larger bit depth than that of a standard SLM (8-bit). Furthermore, to consolidate and verify the azimuthal index measurement precision of 2×10^{-5} demonstrated here, a 16-bit SLM is required to achieve an azimuthal index step size at this level. That is, the azimuthal index measurement precision demonstrated here is already at the limit of what is possible using the highest bit-depth SLM commercially available, a 16-bit SLM (for example, Meadowlark Optics, HSPDM512 1064-PCIe 16-bit). SLMs with such a high bit-depth are not common and thus pose a challenge to test with this approach. We note direct-write lithography for microfabrication with such a high bit-depth may be an alternative approach for fine control of holograms of specific azimuthal index (e.g. the DWL 66+ Laser Lithography System has a grayscale capability of 65,536 levels). We utilise this determination of azimuthal index to measure the refractive index of the sucrose solution surrounding the SPP, achieving a best precision of 6.4×10^{-7} RIU. This compares favourably to existing commercial and research technologies. Commercial refractometers typically utilise total internal reflection, achieving precision of 10^{-5} RIU. Comparing our approach more broadly, plasmonic refractive index sensors[62,63] reach precisions of 10^{-6} RIU, but often have limited measurement range due to properties of the plasmonic structure. Whispering gallery optical resonators have achieved a precision of 2.8×10^{-7} RIU[64], while polarization-dependent absorption of graphene has achieved 1.7×10^{-8} RIU precision, enabling single cell detection[65]. A summary of previous studies being found in Supplementary Table 5. The precision of our refractive index measurements can be improved by increasing the azimuthal index of the generated beam via two routes: utilising shorter wavelengths and using SPPs with greater heights. Moving to a laser wavelength of 385 nm and a SPP height of 258.5 µm would lead to a 30-fold improvement to the refractive index measurements compared to our 1064 nm measurement with SPP5. This would enable a measurement precision of 3×10^{-8}. See the Supplementary Information, Sections 2.1 and 2.2 for a more detailed discussion.

To demonstrate the potential of our approach for biological studies, we measured the refractive index of haemoglobin. Haemoglobin, the oxygen-binding protein found within red blood cells, is responsible for transporting oxygen throughout the body, and its optical properties, including refractive index, are of diagnostic relevance[66]. Specifically, the refractive index of haemogloin is noted as an indicator of health and is presently a challenging parameter to measure accurately[67]. Our study showed agreement of the refractive index of haemoglobin to within 0.02% of that measured with a commercial refractometer, which also agrees with literature values[68]. Additionally, we recorded the refractive index of haemoglobin across a range of concentrations, with results consistent with previously reported values[69]. Our demonstrated capability to perform these measurements with high accuracy in such miniscule sample volumes offers a valuable approach for precise optical characterisation that may be extended to other liquid or gaseous analytes in future studies. Specifically, measurements of refractive index are not only of importance for biology but may also serve as a quality control parameter in industries such as food and beverage production (e.g. sugar content of drinks), pharmacology, or chemical analysis[63,70].

The microfluidic environment within which the refractive index measurements were undertaken is worthy of discussion. We used a chamber with a sample volume of 22 µL, within which the SPP and laser sampled a dramatically smaller volume of approximately 300 pL. We

https://doi.org/10.1038/s41467-026-72281-3

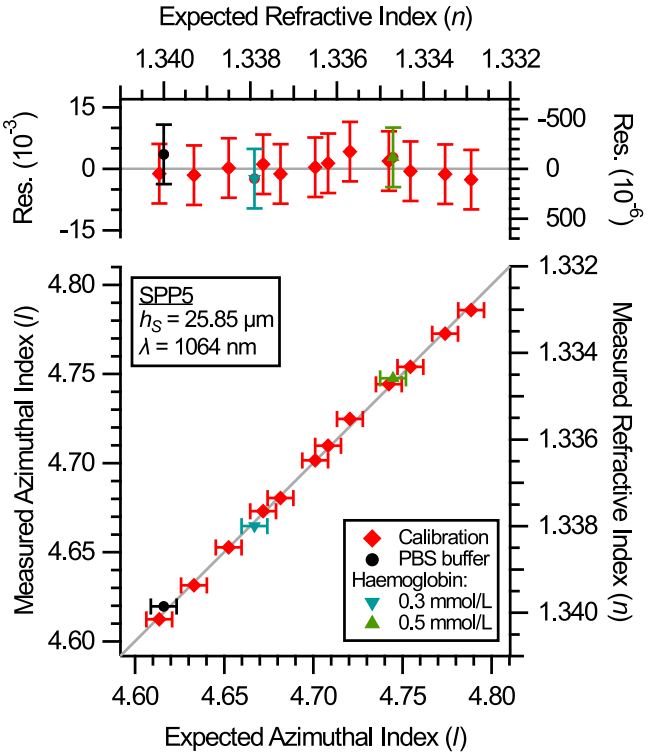

Fig. 4 | Study of biological measurements based on haemoglobin. Haemoglobin measurements are shown in black, green, cyan using SPP5 with a plate height h_s = 25.85 µm at a wavelength of λ = 1064 nm. Measured azimuthal index as a function of the expected azimuthal index, as well as the extracted refractive index measurements. The upper panel shows the precision of the measurements by presenting residuals between the measurements and the expected values. Each calibration point comprises of one sample (N = 1). Each biological measurement (PBS and haemoglobin) consists of one sample (N = 1). The error bars represent the measurement accuracy of the commercial refractometer (±3 × 10^{-4} RIU).

expect that the total sample volume could be reduced to 50 pL by designing the chamber to match the volume sampled by the SPP and laser. The sample volume is limited by the physical footprint of the optical element that converts refractive index to a measurable optical quantity, in this case, the azimuthal index. Accordingly, smaller optical elements, such as metasurfaces, provide a pathway toward substantially reduced sample volumes. Metasurfaces, such as subwavelength nano-pillar quadrumer, may offer a route for a reduction in sample volume to hundreds of attolitres[71]. Reducing the sample volume would result in the measurement being more tolerant of refractive index gradients. A theoretical analysis from our work, presented in the Supplementary Information, Section 1.3, shows that a 0.1% refractive index gradient across SPP5, corresponding to 0.024 RIU/pL, would create a ±1% offset in the refractive index measurement. Turning to miniaturisation of the optical footprint, improved stability could be attained by utilising an SPP directly printed onto the distal end of an optical fibre[72]. Importantly, our scheme could be used to overcome challenges associated with biological samples that are found in extremely low quantities, allowing for ultra-low volume measurements of nucleic acids[73] or low molecular weight compounds[74]. The application of refractive index measurements in single-cell protein analysis[75] suggests a promising avenue for further study in these areas.

To increase throughput and enable detection of spatial variations in refractive index, multiple measurements could be made on a single chip, see Section 9 of the Supplementary Information. This could be achieved either with arrays of SPPs in parallel microfluidic channels to measure multiple samples simultaneously, or by integrating multiple SPPs within a single chamber to measure spatial variations in refractive index within a sample. Each SPP could be interrogated either sequentially or simultaneously by assigning distinct interrogation wavelengths to each SPP and separating the outputs with wavelength filtering after the sample, for example, using an optical frequency comb as the light source. Furthermore, these refractive index measurements can be taken at high speeds, only limited by the exposure time of the camera to ensure the speckle pattern is captured with sufficient SNR, enabling real-time measurements. For the demonstration here, the exposure time used was 20 ms, leading to a 50 Hz measurement rate, which could be improved with a higher-quality camera or higher optical power. In a microfluidic environment, refractive index gradients can be highly informative. For example, spatio-temporal differences in refractive index occur during early embryo development, and measurement of other such gradients critical in immune cell response, and its relevance to the development of metastatic cancer would be interesting to investigate[76,77]. Additionally, refractive index gradients in microfluidic environments can identify molecular transport (mixing) between adjacent laminar flows and allow investigation of molecular diffusion at flow boundaries[78–80]. Integrating real-time refractive index measurements into a multiplexed microfluidic system would allow monitoring of refractive index gradients as a biological system evolves.

In summary, we have demonstrated refractive index measurements of unprecedented precision in ultra-low sample volumes, enabled by speckle-based determination of the fractional azimuthal index. This approach outperforms existing commercial systems and is highly competitive with other research-grade refractometers, but also offers a scalable platform for multiplexed, high-speed measurements in a microfluidic environment. The ability to resolve refractive index gradients in real time opens new opportunities for studying dynamic biological processes, such as molecular diffusion and protein signalling, as well as for monitoring chemical and industrial systems where quality control is critical. By combining very-high sensitivity with the potential for miniaturisation, high throughput, and spatio-temporal resolution, our methodology establishes a new application by utilising precision measurement of light fields with orbital angular momentum. This offers a foundation for next-generation refractive index sensing across the natural sciences.

Methods

Spiral phase plate (SPP) fabrication

Computer-aided design software (CAD), SolidWorks (Dassault Systémes), was used to generate parametric three-dimensional model geometries and exported to STL format. STL files were imported into the computer-aided manufacturing (CAM) software, DeScribe (Nanoscribe GmbH). The devices were sliced in fixed mode as solid bodies, using a single contour, with a hatching distance of 100 nm, and hatching angle of 90°. Optimal layer heights were selected for each spiral ramp height (h_s), with the maximum edge length of any horizontal layer plane kept below 200 nm, ensuring smooth spiral ramp surfaces. The exposure parameters were individually optimised for each layer height, using variable exposure mode with optimal parameters outlined in Supplementary Table 7. The devices were printed as solid bodies using the Nanoscribe Photonic Professional GT+ operating in dip-in mode with IP-DIP resin deposited onto a 25 mm square fused silica slide. The printer was equipped with a 63× magnification objective (all Nanoscribe GmbH). Following exposure, devices were developed in approximately 20 mL of SU-8 developer (Kayaku Advanced Materials Inc.) for approximately 6 min, and blow dried with nitrogen. The resulting SPP were imaged with a scanning electron microscope, which is shown in Fig. 1c). The fabrication accuracy is discussed in the Supplementary Information, Section 3.4. The refractive index of the SPP polymer at 1064 nm is n_{SPP} = 1.53 RIU[81,82], and at the wavelength of 532 nm the refractive index is n_{SPP} = 1.55 RIU[81,82]. This

https://doi.org/10.1038/s41467-026-72281-3

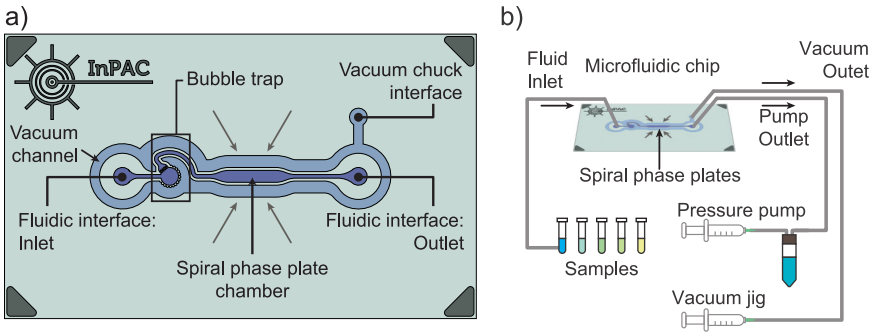

Fig. 5 | Illustration of the microfluidic chip and experimental utilisation. **a** Schematic of the microfluidic chip with marked components. A microscope image of this chip is shown in Fig. 1b). The fluids enter from the inlet and travel through the purple-coloured region that houses the SPPs and later exit through the outlet. The blue-coloured region is connected to the vacuum jig designed to encourage reversible sealing of the PDMS to glass. **b** A single inlet is connected to sample Eppendorf's containing liquid samples of different refractive index through Tygon tubing. The fluid outlet is connected to a basic negative pressure pump consisting of a syringe and 50 mL Falcon tube. Vacuum is supplied by a drawn 50 mL syringe held open by a jig. Withdrawing air from the pressure pump creates a pressure differential driving flow. Withdrawal of 1 mL of air is sufficient to maintain flow rates of approximately 50 µL/min for the duration of the experiment, while fluid switching is achieved by clamping the inlet during transfer between sample tubes.

resist has well-known mechanical and thermal stability[83], and is stable in contact with water or other biological fluids[84]. Further discussion on the refractive index wavelength dependence[85], along with thermal expansion properties[86], of IP-DIP is discussed in more detail in the Supplementary Information, Sections 3.2 and 3.5, respectively.

Fabrication of the microfluidic chamber

The microfluidic system is based on polydimethylsiloxane (PDMS) polymer (SYLGARD™ 184, Dow Corning), fabricated using standard photolithography techniques[87]. Channel structures are patterned into the underside of a PDMS slab through casting onto a template. The negative template consisted of a raised SU-8 3050 photoresist (Kayaku Advanced Materials Inc.) structures patterned on a flat Silicon wafer substrate. SU-8 3050 was spin-coated at 850 rpm for 30 s (Karl Süss RC8) onto a 4-inch silicon wafer to a thickness of 160 µm, the SU-8 was then soft baked on a levelled hotplate (CAT Scientific MCS-78) for 40 min to remove solvents before patterning using a maskless aligner (MLA 150, Heidelberg instruments) with an exposure wavelength of 375 nm, dose of 600 mJ/cm^2, and defocus set to 20. Crosslinking of patterned resist was initiated with a post-exposure bake at 90° for 5 min, followed by removal of unexposed resist through sonication in SU-8 developer. The wafer was hard baked for 12 min at 175° to increase mechanical stability and remove residual solvents, then silanized to aid with mould release, through exposure to trichloro(1,1,2,2-perfluoocytl) silane (Sigma-Aldrich) vapour for 8 min in a desiccator, resulting in a robust, re-usable mould for PDMS casting.

PDMS prepolymer was mixed in a planetary centrifugal vacuum mixer (THINKY ARV-310) with curing agent in a 1:10 ratio by weight. PDMS was cast on the master template and cured at 130 °C in a convection oven for 25 min. The cured PDMS was peeled off the mould, cut to size, and punched with 0.75 mm interface holes. The system consisted of a single fluid channel, with an expanded chamber that is placed over a set of SPPs, (see the schematic in Fig. 5a). A bubble trap [88] was included prior to the phase plate chamber to reduce the impact of bubbles that may otherwise cause unwanted scattering of the beam. The fluidic system included an integrated vacuum chuck (offset channels) facilitating bubble absorption and easy reuse through substrate changeover, with negative pressure applied through an attached syringe housed in a custom-built jig, (see the schematic in Fig. 5b). The PDMS chip was aligned with SPPs using a dissecting microscope, and flow was achieved by connecting a negative pressure pump to the channel outlet. The flow rate in the microfluidics channels was set at 2 cc/min, this rate can be lowered or increased by changing the pressure in the negative pressure pump.

Sucrose solution preparation

Sucrose solutions of various refractive indices were prepared by mixing sucrose with water. For example, a 5% by mass sucrose solution (5% by mass sucrose solution, known as 5 brix), 5 g of sucrose (Chemsupply sucrose) was mixed with 95 g of Mili-Q water (Merk Mili-Q-IQ 7000). The solution was mixed on a magnetic stirrer (IKA, RCT basic). The refractive index of each of the sucrose solutions made was checked using a handheld refractometer (MyBrix, Mettler Toledo). These solutions were then stored in a 100 mL capped glass bottle for repeated use. Prior to the experiment, the solutions were filtered with a 0.22 µm syringe filter (Millex Millipore) into a 1.5 mL Eppendorf tube. The refractive index of the samples was remeasured every time at the start of the experiment to ensure any changes in the refractive index over time were taken into account. The sucrose samples refractive index dependence upon wavelength[89–92] and temperatures[93] is discussed in more detail in the Supplementary Information, Sections 3.1 and 3.3, respectively.

Haemoglobin samples preparation

Ferrous haemoglobin (H0267, Sigma Aldrich) was dissolved in phosphate- buffered saline (PBS) to concentrations of 0.3 mmol/L and 0.5 mmol/L. Samples were briefly vortexed and filtered using a 0.22 µm filter (Millex Millipore). A blank sample containing only PBS was also prepared. New samples were prepared prior to the start of each experiment, and the refractive index verified with a commercial refractometer (MyBrix, Mettler Toledo). The haemoglobin samples refractive index dependence upon temperatures[94] is discussed in more detail in the Supplementary Information, Section 3.3.

Optical measurements

The laser source used was IRCL-300-1064-S, CrystaLaser LC for measurements at 1064 nm, which was focused onto the SPP using a plano-convex lens with a 100 mm focal length (AC254-100-B-ML, Thorlabs), as seen in Fig. 1a). The SPP converts the input Gaussian spatial profile laser beam into a LG beam shape. The transmission of such an SPP is greater than 95%. An aspheric Lens with a 11 mm focal length (C220TMD-B, Thorlabs) was used to image the converted LG beam onto the camera imaging the beam. A charge-coupled device (CCD) camera (EO-1312M, Edmund Optics) and a complementary metal-oxide-semiconductor (CMOS)-camera (Alvium 1800 u-158m, Allied Vision) are used for the detection of the beam profile and speckle

patterns, respectively, which were recorded with manufacture software. The effect of camera noise[95] upon the measurement is discussed in the Supplementary Information, Section 4.4. The speckle pattern was generated using a disordered medium in front of the CMOS camera—in our case, this was a piece of scotch tape with a 40 μm thickness.

For the measurements at input wavelength of 532 nm a second harmonic generator (WH-0532-000-F-B-C) was used to convert a 1064 nm laser source (Coherent Mephisto 2000) into one at 532 nm. For a fair comparison, special care was taken to ensure that the beam size at the SPP was the same for both wavelengths; this was achieved by changing the beam size before the 100 mm lens. It is also worth mentioning that when operating at a wavelength of 532 nm, the optics were switched to their counterparts with anti-reflection coatings at 532 nm.

The first step was to calibrate the system in a desired range of refractive indicies, for this, sucrose solutions of known refractive index were used. Calibrating the system with 11 different sucrose solutions was found to be sufficient to reliably calibrate the PCA algorithm, as well as to keep the duration of the experiment small to minimise any drifting, which may result in calibration errors. These samples were introduced through the microfluidic environment, which housed the SPP. Since the SPP was immersed in a sample of interest with a particular refractive index, the produced LG beam depended on the refractive index, and consequently, the speckle pattern depends on the refractive index of the sample as described by Eq. 2. Once the calibration in a particular region was achieved, the refractive index of any unknown solution in that region could be determined.

Determining the azimuthal index and refractive index using speckle

The azimuthal index was determined based on the generated speckle patterns, which were analysed with the PCA[96]. To calibrate the PCA and determine the transformation matrix to extract the first principal component, a range of sucrose media with different refractive indices was passed through the microfluidic chip, immersing the SPPs. This typically consisted of a image for 11 sucrose media of different refractive indices, which were used to calibrate the PCA to determine the transformation matrix and extract the first principal component of the data. Typically, principal component 1 contained ≈90% of the variance of the data, highlighting that the PCA is only dependent upon the change in azimuthal index and other environmental changes are not relevant to this analysis. The first principal component was compared to the known refractive index measured by using the commercial refractometer, with a fit to these two data sets taking the form of a linear relationship. With the calibrated transformation matrix, the samples of unknown refractive index values were measured, with their imaged speckle patterns input into the PCA and the refractive index produced. Unknown refractive index samples were able to be measured via interpolation between calibration points due to the linearity of the PCA analysis and the known relationship between the first principal component and refractive index. A detailed theoretical analysis of the PCA process is presented in the Supplementary Information, Section 1.

While the precision measurements presented here are between refractive indices from 1.332 to 1.340, this method has been tested over a wider range of refractive index changes from 1.330 to 1.440, measured over a 2 h time frame, with the results showing similar agreements to the smaller ranges shown here. This is a relevant refractive index range for biological studies. For higher refractive index samples, the sucrose solutions being used become highly viscous and difficult to use with the microfluidic system utilised here. As a result of this, we limited our range of refractive index measurements to those presented above. We note that other solutions exist[97] that have higher refractive indices, if a broader refractive index measurement range is required.

Reporting summary

Further information on research design is available in the Nature Portfolio Reporting Summary linked to this article.

Data availability

The data presented in Figures 2–4 of this study have been deposited in the FigShare database[98].

References

1. Allen, L., Beijersbergen, M. W., Spreeuw, R. & Woerdman, J. Orbital angular momentum of light and the transformation of Laguerre-Gaussian laser modes. *Phys. Rev. A* **45**, 8185 (1992).
2. Cheng, M., Jiang, W., Guo, L., Li, J. & Forbes, A. Metrology with a twist: probing and sensing with vortex light. *Light Sci. Appl.* **14**, 4 (2025).
3. Yao, A. M. & Padgett, M. J. Orbital angular momentum: origins, behavior and applications. *Adv. Opt. Photonics* **3**, 161–204 (2011).
4. Allen, L., Padgett, M. & Babiker, M. Iv the orbital angular momentum of light. in *Progress in Optics*, Vol. 39, 291–372 (Elsevier, 1999).
5. Rosales-Guzmán, C., Ndagano, B. & Forbes, A. A review of complex vector light fields and their applications. *J. Opt.* **20**, 123001 (2018).
6. Padgett, M. & Allen, L. The poynting vector in Laguerre-Gaussian laser modes. *Opt. Commun.* **121**, 36–40 (1995).
7. Padgett, M. & Bowman, R. Tweezers with a twist. *Nat. Photonics* **5**, 343–348 (2011).
8. Willner, A. E. et al. Optical communications using orbital angular momentum beams. *Adv. Opt. Photonics* **7**, 66–106 (2015).
9. Wang, J. et al. Terabit free-space data transmission employing orbital angular momentum multiplexing. *Nat. Photonics* **6**, 488–496 (2012).
10. Mair, A., Vaziri, A., Weihs, G. & Zeilinger, A. Entanglement of the orbital angular momentum states of photons. *Nature* **412**, 313–316 (2001).
11. Sit, A. et al. High-dimensional intracity quantum cryptography with structured photons. *Optica* **4**, 1006–1010 (2017).
12. Willig, K. I., Rizzoli, S. O., Westphal, V., Jahn, R. & Hell, S. W. STED microscopy reveals that synaptotagmin remains clustered after synaptic vesicle exocytosis. *Nature* **440**, 935–939 (2006).
13. Scheiderer, L., Marin, Z. & Ries, J. Minflux achieves molecular resolution with minimal photons. *Nat. Photonics* **19**, 238–247 (2025).
14. Lukinavičius, G. et al. Stimulated emission depletion microscopy. *Nat. Rev. Methods Primers* **4**, 56 (2024).
15. Zhang, H. et al. Review on fractional vortex beam. *Nanophotonics* **11**, 241–273 (2021).
16. Gibson, G. et al. Free-space information transfer using light beams carrying orbital angular momentum. *Opt. Express* **12**, 5448–5456 (2004).
17. Galvez, E., Coyle, L., Johnson, E. & Reschovsky, B. Interferometric measurement of the helical mode of a single photon. *New J. Phys.* **13**, 053017 (2011).
18. Ren, Z.-C., Cheng, Z.-M., Wang, X.-L., Ding, J. & Wang, H.-T. Polarization interferometric prism: a versatile tool for generation of vector fields, measurement of topological charges, and implementation of a spin–orbit controlled-not gate. *Appl. Phys. Lett.* **118**, 011105 (2021).
19. Wang, M. et al. Spin-orbit-locked hyperbolic polariton vortices carrying reconfigurable topological charges. *eLight* **2**, 12 (2022).
20. Leach, J., Padgett, M. J., Barnett, S. M., Franke-Arnold, S. & Courtial, J. Measuring the orbital angular momentum of a single photon. *Phys. Rev. Lett.* **88**, 257901 (2002).

21. Sztul, H. & Alfano, R. Double-slit interference with Laguerre-Gaussian beams. *Opt. Lett.* **31**, 999–1001 (2006).
22. Mourka, A., Baumgartl, J., Shanor, C., Dholakia, K. & Wright, E. M. Visualization of the birth of an optical vortex using diffraction from a triangular aperture. *Opt. Express* **19**, 5760–5771 (2011).
23. Huang, H.-C., Lin, Y.-T. & Shih, M.-F. Measuring the fractional orbital angular momentum of a vortex light beam by cascaded Mach–Zehnder interferometers. *Opt. Commun.* **285**, 383–388 (2012).
24. Li, X., Tai, Y., Lv, F. & Nie, Z. Measuring the fractional topological charge of LG beams by using interference intensity analysis. *Opt. Commun.* **334**, 235–239 (2015).
25. Xu, J. et al. Topological charge recognition of vortex beams using PDs. *IEEE Photonics Technol. Lett.* **36**, 1461–1464 (2024).
26. Liu, Z., Yan, S., Liu, H. & Chen, X. Superhigh-resolution recognition of optical vortex modes assisted by a deep-learning method. *Phys. Rev. Lett.* **123**, 183902 (2019).
27. Jing, G. et al. Recognizing fractional orbital angular momentum using feed forward neural network. *Results Phys.* **28**, 104619 (2021).
28. Shikder, A. & Nishchal, N. K. Measurement of the fractional topological charge of an optical vortex beam through interference fringe dislocation. *Appl. Opt.* **62**, D58–D67 (2023).
29. Cao, M. et al. Machine learning based accurate recognition of fractional optical vortex modes in atmospheric environment. *Appl. Phys. Lett.* **119**, 141103 (2021).
30. Deng, D., Lin, M., Li, Y. & Zhao, H. Precision measurement of fractional orbital angular momentum. *Phys. Rev. Appl.* **12**, 014048 (2019).
31. Zhu, J. et al. Probing the fractional topological charge of a vortex light beam by using dynamic angular double slits. *Photonics Res.* **4**, 187–190 (2016).
32. Zheng, S. & Wang, J. Measuring orbital angular momentum (OAM) states of vortex beams with annular gratings. *Sci. Rep.* **7**, 40781 (2017).
33. Metzger, N. K. et al. Harnessing speckle for a sub-femtometre resolved broadband wavemeter and laser stabilization. *Nat. Commun.* **8**, 15610 (2017).
34. Bruce, G. D., O'Donnell, L., Chen, M. & Dholakia, K. Overcoming the speckle correlation limit to achieve a fiber wavemeter with attometer resolution. *Opt. Lett.* **44**, 1367–1370 (2019).
35. Trivedi, V. et al. 3D printed hand-held refractometer based on laser speckle correlation. *Opt. Lasers Eng.* **118**, 7–13 (2019).
36. Tran, V., Sahoo, S. K., Wang, D. & Dang, C. Utilizing multiple scattering effect for highly sensitive optical refractive index sensing. *Sens. Actuators A Phys.* **301**, 111776 (2020).
37. Barrios, C. A. Highly sensitive refractometric sensing system based on the combination of lensing and laser speckle correlation. *Opt. Lasers Eng.* **177**, 108122 (2024).
38. Facchin, M., Bruce, G. D. & Dholakia, K. Measuring picometre-level displacements using speckle patterns produced by an integrating sphere. *Sci. Rep.* **13**, 14607 (2023).
39. Mazilu, M., Mourka, A., Vettenburg, T., Wright, E. M. & Dholakia, K. Simultaneous determination of the constituent azimuthal and radial mode indices for light fields possessing orbital angular momentum. *Appl. Phys. Lett.* **100**, 231115 (2012).
40. Bianchetti, A., Etchepareborda, P. & Federico, A. Determining the fractional topological charge shifting in perfect vortices from laser speckle. *Opt. Commun.* **441**, 74–79 (2019).
41. Fickler, R., Ginoya, M. & Boyd, R. W. Custom-tailored spatial mode sorting by controlled random scattering. *Phys. Rev. B* **95**, 161108 (2017).
42. Gong, L. et al. Optical orbital-angular-momentum-multiplexed data transmission under high scattering. *Light Sci. Appl.* **8**, 27 (2019).
43. Zhang, Z., Yin, X., Liu, Y., Wang, Y. & Xin, X. Efficient sorting for an orbital angular momentum multiplexing communication link based on a digital micromirror device and a diffuser. *Opt. Express* **30**, 6203–6215 (2022).
44. Ma, R. et al. Orbital-angular-momentum-dependent speckles for spatial mode sorting and demultiplexing. *Optica* **11**, 595–605 (2024).
45. Dorrah, A. H., Zamboni-Rached, M. & Mojahedi, M. Experimental demonstration of tunable refractometer based on orbital angular momentum of longitudinally structured light. *Light Sci. Appl.* **7**, 40 (2018).
46. Kerschbaumer, N. M. et al. Twisted light Michelson interferometer for high precision refractive index measurements. *Opt. Express* **30**, 29722–29734 (2022).
47. Meglinski, I., Lopushenko, I., Sdobnov, A. & Bykov, A. Phase preservation of orbital angular momentum of light in multiple scattering environment. *Light Sci. Appl.* **13**, 214 (2024).
48. Wu, S., Ma, F. & Wang, A. Detecting small variation rate of refractive index based on OAM interferometry and time–frequency analysis. *Opt. Laser Technol.* **174**, 110566 (2024).
49. Liu, E. et al. Oam mode-excited surface plasmon resonance for refractive index sensing based on a photonic quasi-crystal fiber. *J. Opt. Soc. Am. B* **38**, F16–F22 (2021).
50. Baniasadi, M. & Ghasempour Ardakani, A. Refractive index sensing using analytical calculation of angular momentum sidebands of a Laguerre-Gaussian beam reflected from a plasmonic structure. *Sci. Rep.* **15**, 20689 (2025).
51. Beijersbergen, M., Coerwinkel, R., Kristensen, M. & Woerdman, J. Helical-wavefront laser beams produced with a spiral phaseplate. *Opt. Commun.* **112**, 321–327 (1994).
52. Caño-García, M., Quintana, X., Otón, J. & Geday, M. A. Dynamic multilevel spiral phase plate generator. *Sci. Rep.* **8**, 15804 (2018).
53. de la Rosa, P. et al. Generation of integer and fractional vortex beams based on liquid crystal electronically reconfigurable spiral phase plates. *Opt. Express* **31**, 31212–31220 (2023).
54. Facchin, M., Khan, S. N., Dholakia, K. & Bruce, G. D. Determining intrinsic sensitivity and the role of multiple scattering in speckle metrology. *Nat. Rev. Phys.* **6**, 500–508 (2024).
55. Kedenburg, S., Vieweg, M., Gissibl, T. & Giessen, H. Linear refractive index and absorption measurements of nonlinear optical liquids in the visible and near-infrared spectral region. *Opt. Mater. Express* **2**, 1588–1611 (2012).
56. Hu, X.-B., Dong, M.-X., Zhu, Z.-H., Gao, W. & Rosales-Guzmán, C. Does the structure of light influence the speckle size? *Sci. Rep.* **10**, 199 (2020).
57. Li, X. et al. Study on properties of speckle field formed by Laguerre-Gaussian beam illumination. *Acta Opt. Sin.* **35**, 726001 (2015).
58. Zhao, H., Brown, P. H. & Schuck, P. On the distribution of protein refractive index increments. *Biophys. J.* **100**, 2309–2317 (2011).
59. Seki, A., Narita, K. & Watanabe, K. Refractive index measurement in sucrose solution and beverage using surface plasmon resonance sensor based on hetero-core structured fiber optic. *Procedia Chem.* **20**, 115–117 (2016).
60. Mohan, S., Kato, E., Drennen III, J. K. & Anderson, C. A. Refractive index measurement of pharmaceutical solids: a review of measurement methods and pharmaceutical applications. *J. Pharm. Sci.* **108**, 3478–3495 (2019).
61. Matveyeva, T., Sarimov, R. M. & Binhi, V. N. Precision interferometry as a new method for studying the conformational state of protein and its interaction with a solvent. *Opt. Spectrosc.* **128**, 771–777 (2020).
62. White, I. M. & Fan, X. On the performance quantification of resonant refractive index sensors. *Opt. Express* **16**, 1020–1028 (2008).

63. Xu, Y. et al. Optical refractive index sensors with plasmonic and photonic structures: promising and inconvenient truth. *Adv. Opt. Mater.* **7**, 1801433 (2019).
64. Li, H. & Fan, X. Characterization of sensing capability of optofluidic ring resonator biosensors. *Appl. Phys. Lett.* **97**, 011105 (2010).
65. Xing, F. et al. Ultrasensitive flow sensing of a single cell using graphene-based optical sensors. *Nano Lett.* **14**, 3563–3569 (2014).
66. Serebrennikova, Y. M., Huffman, D. E. & Garcia-Rubio, L. H. Characterization of red blood cells with multiwavelength transmission spectroscopy. *Biomed. Res. Int.* **2015**, 382641 (2015).
67. Alizamir, A., Gholami, A., Bahrami, N. & Ostadhassan, M. Refractive index of hemoglobin analysis: a comparison of alternating conditional expectations and computational intelligence models. *ACS Omega* **7**, 33769–33782 (2022).
68. Zhernovaya, O., Sydoruk, O., Tuchin, V. & Douplik, A. The refractive index of human hemoglobin in the visible range. *Phys. Med. Biol.* **56**, 4013 (2011).
69. Jin, Y., Chen, J., Xu, L. & Wang, P. Refractive index measurement for biomaterial samples by total internal reflection. *Phys. Med. Biol.* **51**, N371 (2006).
70. Jaywant, S. A., Singh, H. & Arif, K. M. Sensors and instruments for brix measurement: a review. *Sensors* **22**, 2290 (2022).
71. Chen, Q. et al. Highly efficient vortex generation at the nanoscale. *Nat. Nanotechnol.* **19**, 1000–1006 (2024).
72. Weber, K. et al. Single mode fiber based delivery of OAM light by 3D direct laser writing. *Opt. Express* **25**, 19672–19679 (2017).
73. Desjardins, P. & Conklin, D. Nanodrop microvolume quantitation of nucleic acids. *J. Vis. Exp.* **45**, 2565 (2010).
74. Davis, T. M. & Wilson, W. Determination of the refractive index increments of small molecules for correction of surface plasmon resonance data. *Anal. Biochem.* **284**, 348–353 (2000).
75. Zhang, Q. et al. Quantitative refractive index distribution of single cell by combining phase-shifting interferometry and AFM imaging. *Sci. Rep.* **7**, 2532 (2017).
76. Keenan, T. M. & Folch, A. Biomolecular gradients in cell culture systems. *Lab Chip* **8**, 34–57 (2008).
77. Dwapanyin, G. O. et al. Investigation of refractive index dynamics during in vitro embryo development using off-axis digital holographic microscopy. *Biomed. Opt. Express* **14**, 3327–3342 (2023).
78. Squires, T. M. & Quake, S. R. Microfluidics: fluid physics at the nanoliter scale. *Rev. Mod. Phys.* **77**, 977–1026 (2005).
79. Sung, Y. et al. Three-dimensional holographic refractive-index measurement of continuously flowing cells in a microfluidic channel. *Phys. Rev. Appl.* **1**, 014002 (2014).
80. Costin, C. D. & Synovec, R. E. Measuring the transverse concentration gradient between adjacent laminar flows in a microfluidic device by a laser-based refractive index gradient detector. *Talanta* **58**, 551–560 (2002).
81. Gissibl, T., Wagner, S., Sykora, J., Schmid, M. & Giessen, H. Refractive index measurements of photo-resists for three-dimensional direct laser writing. *Opt. Mater. Express* **7**, 2293–2298 (2017).
82. Dottermusch, S., Busko, D., Langenhorst, M., Paetzold, U. W. & Richards, B. S. Exposure-dependent refractive index of nanoscribe IP-dip photoresist layers. *Opt. Lett.* **44**, 29–32 (2019).
83. Rohbeck, N. et al. Effect of high strain rates and temperature on the micromechanical properties of 3D-printed polymer structures made by two-photon lithography. *Mater. Des.* **195**, 108977 (2020).
84. Larramendy, F. et al. 3D arrays of microcages by two-photon lithography for spatial organization of living cells. *Lab Chip* **19**, 875–884 (2019).
85. Schmid, M., Ludescher, D. & Giessen, H. Optical properties of photoresists for femtosecond 3D printing: refractive index, extinction, luminescence-dose dependence, aging, heat treatment and comparison between 1-photon and 2-photon exposure. *Opt. Mater. Express* **9**, 4564–4577 (2019).
86. Qu, J., Kadic, M., Naber, A. & Wegener, M. Micro-structured two-component 3D metamaterials with negative thermal-expansion coefficient from positive constituents. *Sci. Rep.* **7**, 40643 (2017).
87. McDonald, J. C. & Whitesides, G. M. Poly (dimethylsiloxane) as a material for fabricating microfluidic devices. *Acc. Chem. Res.* **35**, 491–499 (2002).
88. Lochovsky, C., Yasotharan, S. & Günther, A. Bubbles no more: in-plane trapping and removal of bubbles in microfluidic devices. *Lab Chip* **12**, 595–601 (2012).
89. Ghosh, G. Sellmeier coefficients and dispersion of thermo-optic coefficients for some optical glasses. *Appl. Opt.* **36**, 1540–1546 (1997).
90. Ghosh, G., Endo, M. & Iwasaki, T. Temperature-dependent Sellmeier coefficients and chromatic dispersions for some optical fiber glasses. *J. Lightwave Technol.* **12**, 1338–1342 (1994).
91. Bhar, G. & Ghosh, G. Temperature dependent phase-matched nonlinear optical devices using CdSe and ZnGeP2. *IEEE J. Quantum Electron.* **16**, 843–838 (1980).
92. Purwandari, E., Arkundato, A., Rohman, L., Cahyono, B. E. et al. Analyses of concentration and wavelength dependent refractive index of sugar solution using Sellmeier equation. *J. Phys. Conf. Ser.* **1825**, 012030 (2021).
93. Daimon, M. & Masumura, A. Measurement of the refractive index of distilled water from the near-infrared region to the ultraviolet region. *Appl. Opt.* **46**, 3811–3820 (2007).
94. Lazareva, E. N. & Tuchin, V. V. The temperature dependence of refractive index of hemoglobin at the wavelengths 930 and 1100 nm. In *Saratov Fall Meeting 2015: Third International Symposium on Optics and Biophotonics and Seventh Finnish-Russian Photonics and Laser Symposium (PALS)*, Vol. 9917, 211–219 (SPIE, 2016).
95. Peterkovic, Z. et al. Optimizing image capture for low-light wide-field quantitative fluorescence microscopy. *APL Photonics* **10**, 031102 (2025).
96. Greenacre, M. et al. Principal component analysis. *Nat. Rev. Methods Primers* **2**, 100 (2022).
97. Laskar, J. M., Shravan Kumar, P., Herminghaus, S., Daniels, K. E. & Schröter, M. High refractive index immersion liquid for super-resolution 3D imaging using sapphire-based aplanatic numerical aperture increasing lens optics. *Appl. Opt.* **55**, 3165–3169 (2016).
98. Perrella, C. et al. Speckle-based measurement of the fractional azimuthal index of orbital angular momentum beams for refractive index sensing-datasets for figures 2–4, https://doi.org/10.25909/31549678 (2026).

Acknowledgements

K.D. acknowledges support from the Australian Research Council (FL210100099). This research was supported by the Australian Research Council Centre of Excellence in Optical Microcombs for Breakthrough Science (project number CE230100006) and funded by the Australian Government. Device fabrication was conducted at the RMIT Micro Nano Research Facility (MNRF) in the Victorian Node of the Australian National Fabrication Facility (ANFF). K.R.D. acknowledges support from the National Health and Medical Research Council (APP2029067), K.R.D is supported by a Future Making Fellowship (University of Adelaide), and the Australian Research Council (FT240100291). A.B. is supported by an ARC DECRA fellowship (DE230100964). This work is supported by the US Office of Naval Research Global (N62909-25-1-2029). We acknowledge Alexander Trowbridge for assistance in generating the experimental diagram.

Author contributions

K.D. conceived and supervised the study. A.A.P., C.P. conducted the experiment(s), preliminary measurements by A.Z. A.Z., C.S., A.B. and

A.M. designed and fabricated the spiral phase plates. C.P. developed the speckle analysis approach and analysed the data. M.L., K.R.D. developed the biological studies. K.D., C.P., A.A.P. and C.S. wrote the manuscript with contributions from other authors. All authors reviewed, edited, and approved the manuscript.

Competing interests
The authors declare no competing interests.

Additional information
Supplementary information The online version contains Supplementary material available at https://doi.org/10.1038/s41467-026-72281-3.

Correspondence and requests for materials should be addressed to Kishan Dholakia.

Peer review information : *Nature Communications* thanks the anonymous reviewer(s) for their contribution to the peer review of this work. A peer review file is available.

Reprints and permissions information is available at http://www.nature.com/reprints

Publisher's note Springer Nature remains neutral with regard to jurisdictional claims in published maps and institutional affiliations.

Open Access This article is licensed under a Creative Commons Attribution-NonCommercial-NoDerivatives 4.0 International License, which permits any non-commercial use, sharing, distribution and reproduction in any medium or format, as long as you give appropriate credit to the original author(s) and the source, provide a link to the Creative Commons licence, and indicate if you modified the licensed material. You do not have permission under this licence to share adapted material derived from this article or parts of it. The images or other third party material in this article are included in the article's Creative Commons licence, unless indicated otherwise in a credit line to the material. If material is not included in the article's Creative Commons licence and your intended use is not permitted by statutory regulation or exceeds the permitted use, you will need to obtain permission directly from the copyright holder. To view a copy of this licence, visit http://creativecommons.org/licenses/by-nc-nd/4.0/.

© The Author(s) 2026